

Synthesis and Characterization of Ruthenium and Iron–Ruthenium Prussian Blue Analogues

Jogendra N. Behera, Deanna M. D'Alessandro, Navid Soheilnia, and Jeffrey R. Long*

Department of Chemistry, University of California, Berkeley, California 94720, and Materials Science Division, Lawrence Berkeley National Laboratory, Berkeley California 94720

Received January 24, 2009. Revised Manuscript Received March 13, 2009

The electronic spectra, electrical conductivity, magnetism, and gas adsorption properties of the newly prepared Prussian blue analogues $\text{Fe}_4[\text{Ru}(\text{CN})_6]_3 \cdot 18\text{H}_2\text{O}$ (**2**) and $\text{K}_{1.2}\text{Ru}_{3.6}[\text{Ru}(\text{CN})_6]_3 \cdot 16\text{H}_2\text{O}$ (**3**) are compared with those of Prussian blue itself ($\text{Fe}_4[\text{Fe}(\text{CN})_6]_3 \cdot 14\text{H}_2\text{O}$, **1**). The increase in the degree of electronic localization for the unsymmetrical iron–ruthenium analogue **2** is reflected in a shift of the intervalence charge transfer (IVCT) band to higher energies and an increase in the electrical resistivity. In contrast, the all-ruthenium analogue **3** exhibits a lower-energy IVCT band, as well as the highest electrical conductivity, due to the combined effects of electronic delocalization and the presence of potassium ions. Unlike Prussian blue, the ruthenium and iron–ruthenium analogues show no magnetic ordering transition above 1.8 K. Nitrogen adsorption measurements at 77 K show the dehydrated forms of **2** and **3** to be microporous with BET surface areas of 670 and 325 m^2/g , respectively.

Introduction

Mixed-valence Prussian blues with the general formula $\text{M}_4[\text{M}'(\text{CN})_6]_3 \cdot n\text{H}_2\text{O}$ (where M and M' are tri- and divalent transition metal cations, respectively) and their analogues have attracted significant attention because of their unusual magnetic,¹ electrical,² optical,³ and gas storage⁴ properties. Recent investigations of Prussian blues have been stimulated by a growing interest in multifunctional materials⁵ and a revival in the chemistry of inorganic cyanide compounds.⁶ Owing to the wide range of possible metal ion substitutions and the ability of cyanide to provide an effective pathway for magnetic superexchange, Prussian blue analogues have been very thoroughly investigated for their magnetic properties.¹ In addition, the combination of microporosity and open metal coordination sites has led to a surge of recent interest

in the gas adsorption properties for dehydrated Prussian blue analogues with varying concentrations of framework vacancies.⁴ Contrastingly, there have been few recent studies of the electrical conductivity of such compounds.²

Prussian blue, $\text{Fe}_4[\text{Fe}(\text{CN})_6]_3 \cdot 14\text{H}_2\text{O}$ ($\text{Fe}^{\text{III}}\text{Fe}^{\text{II}}$, **1**), is an example of a Robin and Day class II mixed-valence compound that exhibits semiconducting characteristics.^{2c} The actual electrical conductivity, however, is dependent on the given sample and is determined by the degree of electronic delocalization, in addition to the interactions between metal ions that reflect the stoichiometry of the system.^{2g} Given their more diffuse valence d orbitals, we were interested in probing the effects of incorporating second-row transition metal ions into such

* Corresponding author. E-mail: jrlong@berkeley.edu.

- (1) (a) Mallah, T.; Thiébaud, S.; Verdager, M. *Science* **1993**, *262*, 1554. (b) Entley, W. R.; Girolami, G. S. *Science* **1995**, *268*, 397. (c) Kahn, O. *Nature (London)* **1995**, *378*, 667. (d) Ferlay, S.; Mallah, T.; Ouahès, R. *Nature (London)* **1995**, *378*, 701. (e) Ohkoshi, S.; Abe, Y.; Fujishima, A.; Hashimoto, K. *Phys. Rev. Lett.* **1999**, *82*, 1285. (f) Hatlevik, Ø.; Buschmann, W. E.; Zhang, J.; Manson, J. L.; Miller, J. S. *Adv. Mater.* **1999**, *11*, 914. (g) Holmes, S. M.; Girolami, G. S. *J. Am. Chem. Soc.* **1999**, *121*, 5593. (h) Bleuzen, A.; Lomenech, C.; Escax, V.; Villain, F.; Varret, F.; Moulin, C. C. D.; Verdager, M. *J. Am. Chem. Soc.* **2000**, *122*, 6648. (i) Colacio, E.; Ghazi, M.; Stoeckli-Evans, H.; Loret, F.; Moreno, J. M.; Perez, C. *Inorg. Chem.* **2001**, *40*, 4876. (j) Gütllich, P.; Garcia, Y.; Woike, T. *Coord. Chem. Rev.* **2001**, *219*, 839.
- (2) (a) Robin, M. B. *Inorg. Chem.* **1962**, *1*, 337. (b) Inoue, H.; Yanagisawa, S. *J. Inorg. Nucl. Chem.* **1974**, *36*, 1409. (c) Robin, M. B.; Day, P. *Adv. Inorg. Chem. Radiochem.* **1967**, *10*, 247. (d) Balzani, V.; Juris, A.; Venturi, M.; Campagna, S.; Serroni, S. *Chem. Rev.* **1996**, *96*, 759. (e) Tennakone, K.; Dharmaratne, W. G. D. *J. Phys. C: Solid State Phys.* **1983**, *16*, 5633. (f) Ganguli, S.; Bhattacharya, M. *J. Chem. Soc., Faraday Trans.* **1983**, *179*, 1513. (g) Feldman, B. J.; Murray, R. W. *Inorg. Chem.* **1987**, *26*, 1702. (h) Yamada, S.; Kuwabara, K.; Koumoto, K. *Mater. Sci. Eng.* **1997**, *B49*, 89.
- (3) (a) Kulesza, P. J.; Malik, M. A.; Berrettoni, M.; Giorgetti, M.; Zamponi, S.; Schmidt, R.; Marassi, R. *J. Phys. Chem. B* **1998**, *102*, 1870. (b) Pyrasch, M.; Toutianoush, A.; Jin, W.; Schnepf, J.; Tieke, B. *Chem. Mater.* **2003**, *15*, 245.

- (4) (a) Deshpande, R. S.; Sharp-Goldman, S. L.; Willson, J. L.; Bocarsly, A. B. *Chem. Mater.* **2003**, *15*, 4239. (b) Kaye, S. S.; Long, J. R. *J. Am. Chem. Soc.* **2005**, *127*, 6506. (c) Chapman, K. W.; Southon, P. D.; Weeks, C. L.; Kepert, C. J. *Chem. Commun.* **2005**, *26*, 3322. (d) Culp, J. T.; Matranga, C.; Smith, M.; Bittner, E. W.; Bockrath, B. *J. Phys. Chem. B* **2006**, *110*, 8325. (e) Kaye, S. S.; Long, J. R. *Catal. Today* **2007**, *120*, 311. (f) Kaye, S. S.; Long, J. R. *Chem. Commun.* **2007**, 4486. (g) Culp, J. T.; Natesakhawat, S.; Smith, M. R.; Bittner, E.; Matranga, C.; Bockrath, B. *J. Phys. Chem. C* **2008**, *112*, 7079. (h) Reguera, L.; Krap, C. P.; Balmaseda, J.; Reguera, E. *J. Phys. Chem. C* **2008**, *112*, 15893. (i) Reguera, L.; Balmaseda, J.; Krap, C. P.; Avila, M.; Reguera, E. *J. Phys. Chem. C* **2008**, *112*, 17443. (j) Culp, J. T.; Smith, M. R.; Bittner, E.; Bockrath, B. *J. Am. Chem. Soc.* **2008**, *130*, 12427. (k) Reguera, L.; Reguera, E.; Balmaseda, J.; Rodriguez-Hernandez, J.; Yee-Madeira, H. *J. Porous Mater.* **2008**, *15*, 719.
- (5) (a) Sato, O.; Iyoda, T.; Fujishima, A.; Hashimoto, K. *Science* **1996**, *271*, 49. (b) Sato, O.; Iyoda, T.; Fujishima, A.; Hashimoto, K. *Science* **1996**, *272*, 704. (c) Beauvais, L. G.; Long, J. R. *J. Am. Chem. Soc.* **2002**, *124*, 12096. (d) Ohkoshi, S.-i.; Tokoro, H.; Matsuda, T.; Takahashi, H.; Irie, H.; Hashimoto, K. *Angew. Chem., Int. Ed.* **2007**, *46*, 3238. (e) Kaye, S. S.; Choi, H. J.; Long, J. R. *J. Am. Chem. Soc.* **2008**, *130*, 16921. (f) Li, D.; Clerac, R.; Roubeau, O.; Harte, E.; Mathoniere, C.; Le Bris, R.; Holmes, S. M. *J. Am. Chem. Soc.* **2008**, *130*, 252.
- (6) (a) Dunbar, K. R.; Heintz, R. A. *Prog. Inorg. Chem.* **1997**, *45*, 283. (b) Verdager, M.; Bleuzen, A.; Marvaud, V.; Vaissermann, J.; Seuleiman, M.; Desplanches, C.; Scuiller, A.; Train, C.; Garde, R.; Gelly, G.; Lomenech, C.; Rosenman, I.; Veillet, P.; Cartier, C.; Villain, F. *Coord. Chem. Rev.* **1999**, *190–192*, 1023. (c) Beltran, L. M. C.; Long, J. R. *Acc. Chem. Res.* **2005**, *38*, 325.

compounds, expecting that this might result in an increased electrical conductivity. Here, we report the synthesis of the new ruthenium-containing Prussian blue analogues $\text{Fe}_4[\text{Ru}(\text{CN})_6]_3 \cdot 18\text{H}_2\text{O}$ ($\text{Fe}^{\text{III}}\text{Ru}^{\text{II}}$, **2**) and $\text{K}_{1.2}\text{Ru}_{3.6}[\text{Ru}(\text{CN})_6]_3 \cdot 16\text{H}_2\text{O}$ ($\text{Ru}^{\text{III}}\text{Ru}^{\text{II}}$, **3**) and compare their electronic, magnetic, and gas sorption properties with those of Prussian blue itself.

Experimental Section

Preparation of Compounds. Prussian blue, $\text{Fe}_4[\text{Fe}(\text{CN})_6]_3 \cdot 14\text{H}_2\text{O}$ (**1**), was synthesized according to a literature procedure,⁷ as was $\text{K}_4[\text{Ru}(\text{CN})_6]$.⁸ Water was distilled and deionized using a Milli-Q filtering system.

$\text{Fe}_4[\text{Ru}(\text{CN})_6]_3 \cdot 18\text{H}_2\text{O}$ (2**).** A solution of $\text{K}_4[\text{Ru}(\text{CN})_6]$ (0.200 g, 0.480 mmol) in 100 mL of water was added dropwise to a stirred solution of $\text{Fe}(\text{NO}_3)_3 \cdot 9\text{H}_2\text{O}$ (0.587 g, 1.45 mmol) in 100 mL of water. The resulting precipitate was allowed to stand in the mother liquor for 24 h, collected by filtration, and washed with 3×250 mL of water. The ensuing solid was dried under reduced pressure to afford 0.375 g (48%) of product as a dark purple powder. IR (neat): ν_{CN} 2045 cm^{-1} . Anal. Calcd for $\text{C}_{18}\text{H}_{36}\text{Fe}_4\text{N}_{18}\text{O}_{18}\text{Ru}_3$: C, 16.3; H, 2.8; Fe, 16.8; N, 18.9; Ru, 22.8. Found: C, 16.3; H, 2.9; Fe, 16.5; N, 18.2; Ru, 22.7. Thermogravimetric analysis confirmed the water content of the compound.

$\text{K}_{1.2}\text{Ru}_{3.6}[\text{Ru}(\text{CN})_6]_3 \cdot 16\text{H}_2\text{O}$ (3**).** Solid $\text{Ru}(\text{acac})_3$ (0.250 g, 0.620 mmol; acac^- = acetyl acetonate) was added to a solution of $\text{K}_4[\text{Ru}(\text{CN})_6]$ (0.130 g, 0.310 mmol) in 10 mL of water, and the mixture was stirred for 1 h at room temperature. The resulting reaction mixture was subsequently transferred into a 23-mL PTFE-lined acid-digestion bomb and heated at 175 °C for 4 days. After cooling to room temperature, the resulting solid was collected by filtration following centrifugation. The solid was washed three times with 30 mL of water and dried under reduced pressure to afford 0.162 g (42%) of product as a dark green powder. IR (neat): ν_{CN} 2060 cm^{-1} . Anal. Calcd for $\text{C}_{18}\text{H}_{32}\text{K}_{1.2}\text{N}_{18}\text{O}_{16}\text{Ru}_{6.6}$: C, 14.7; H, 2.3; K, 3.2; N, 17.1; Ru, 45.3. Found: C, 14.4; H, 2.8; K, 3.0; N, 16.2; Ru, 45.4. Thermogravimetric analysis confirmed the water content of the compound.

Physical Measurements. Infrared spectra were recorded on a Nicolet Avatar 360 FTIR spectrophotometer equipped with an attenuated total reflectance accessory. UV–visible–NIR diffuse reflectance spectra were collected using a CARY 5000 spectrophotometer interfaced with Varian Win UV software. The Kubelka–Munk conversion, $F(R)$ vs wavenumber, of the raw diffuse reflectance spectrum (R vs wavenumber) was obtained by applying the formula $F(R) = (1 - R)^2/2R$. It must be noted that this transform creates a linear relationship for the spectral intensity relative to sample concentration and assumes that the sample is infinitely diluted in the nonabsorbing (Spectralon) matrix, that the sample layer is “infinitely thick”, and that the sample has a constant scattering coefficient. Thermogravimetric analyses were carried out at a ramp rate of 0.25 °C/min under a flow of nitrogen using a TA Instruments Thermogravimetric Analyzer 2950. Powder X-ray diffraction data were collected on a Bruker D8 Advance X-ray powder diffractometer using $\text{Cu K}\alpha$ radiation ($\lambda = 1.5418 \text{ \AA}$). DC magnetic susceptibility measurements were performed using a Quantum Design MPMS2 SQUID magnetometer. Gas adsorption measurements were collected using a Micromeritics ASAP 2020 gas sorption analyzer. Carbon, hydrogen and nitrogen analyses were obtained from the Microanalytical Laboratory of the University of California, Berkeley. Potassium, iron and ruthenium analyses were obtained from Columbia Analytical Services, Inc., Laboratories.

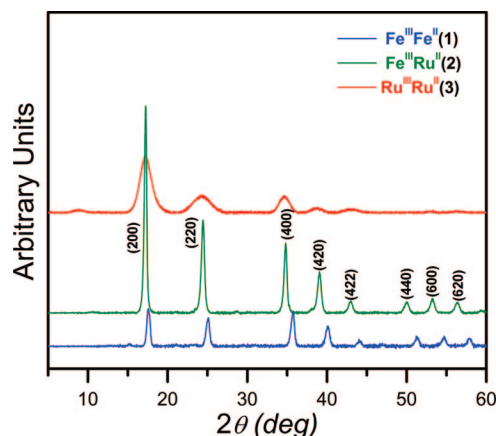


Figure 1. X-ray powder diffraction patterns of the as-synthesized Prussian blue samples of **1** ($\text{Fe}^{\text{III}}\text{Fe}^{\text{II}}$), **2** ($\text{Fe}^{\text{III}}\text{Ru}^{\text{II}}$), and **3** ($\text{Ru}^{\text{III}}\text{Ru}^{\text{II}}$).

Electrical conductivity (DC) measurements were carried out using the standard four-point probe method. The finely powered samples were pressed into rectangular pellets with dimensions of $1 \times 1.64 \times 6 \text{ mm}^3$. The sample had a rectangular shape with two fixed dimensions of 1 and 6 mm. The third dimension was measured using a micrometer. The electrodes were attached by Dotite silver paint, and the distance between the electrodes was measured using an optical microscope. The resistivities of the samples were measured from 130 to 350 K under dynamic vacuum. The custom-designed apparatus employs a Keithley 6221A current source, a Keithley 2182A Nanovoltmeter, and a Cryocon 32B cryogenic temperature controller that are interfaced to a computer via a serial and GPIB connection and automated using LabView software. Current polarization was changed every 0.1 s to subtract any thermal voltage effects. Liquid nitrogen was transferred via a transfer line into a cryostat to permit sample cooling.

Results and Discussion

Synthetic Methods. The conventional precipitation method for the synthesis of Prussian blue analogues involves the dropwise addition of an aqueous solution containing a cation, $[\text{M}(\text{H}_2\text{O})_6]^{x+}$, to an aqueous solution containing an anion, $[\text{M}'(\text{CN})_6]^{y-}$, at room temperature.⁷ While this method was successful in producing $\text{Fe}_4[\text{Ru}(\text{CN})_6]_3 \cdot 18\text{H}_2\text{O}$ (**2**), it failed to generate an all-ruthenium analogue of Prussian blue, presumably owing to the slow ligand exchange rate of $[\text{Ru}(\text{H}_2\text{O})_6]^{3+}$. Consequently, we investigated the use of $\text{Ru}(\text{acac})_3$ under hydrothermal conditions, which indeed provides $\text{K}_{1.2}\text{Ru}_{3.6}[\text{Ru}(\text{CN})_6]_3 \cdot 16\text{H}_2\text{O}$ (**3**).

The infrared spectra of compounds **1–3** (see Figure S1 in the Supporting Information) exhibit characteristic bands for bridging cyanide ligands and solvate water molecules. The sharp bands for ν_{CN} are observed in the 2050–2070 cm^{-1} region, while broad ν_{OH} bands are observed in the range 3200–3500 cm^{-1} and the bending modes for water are observed in the range 1400–1650 cm^{-1} .

Prussian blue analogues exhibit structures based upon the cubic $\text{M}_4[\text{M}'(\text{CN})_6]_3 \cdot n\text{H}_2\text{O}$ framework, wherein octahedral $[\text{M}'(\text{CN})_6]^{4-}$ complexes are linked via octahedrally coordinated, nitrogen-bound M^{3+} ions. The crystallinity of the newly formed products **2** and **3** was confirmed by X-ray powder diffraction analysis. Figure 1 shows a typical powder diffraction pattern, which can be readily indexed as a face-centered cubic phase with space group $Fm\bar{3}m$. Estimated unit

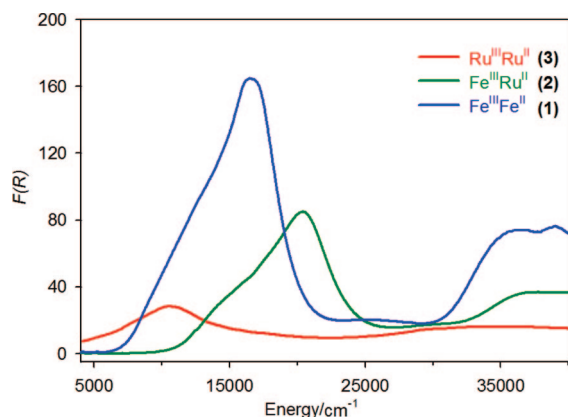
(7) Ludi, A.; Güdel, H. U. *Struct. Bonding (Berlin)* **1973**, *14*, 1.

(8) Krause, R. A.; Violette, C. *Inorg. Chim. Acta* **1986**, *113*, 161.

Table 1. Physical Properties of the Prussian Blues 1–3

compound	lattice constant (Å)	band manifold (cm ⁻¹)	magnetic moment (μ_B) ^a	BET surface area ^b (m ² /g)	H ₂ uptake ^{b,c} (wt %)	electrical conductivity ^d (S/cm)
Fe ₄ [Fe(CN) ₆] ₃ ·14H ₂ O (1)	10.16	16 210	5.76	550	1.2	5.57 × 10 ⁻⁵
Fe ₄ [Ru(CN) ₆] ₃ ·18H ₂ O (2)	10.42	20 180	5.72	670	1.4	5.05 × 10 ⁻⁶
K _{1.2} Ru _{3.6} [Ru(CN) ₆] ₃ ·16H ₂ O (3)	~10.6 ^e	9980	1.69	325	0.5	5.69 × 10 ⁻³

^a This is per M^{III} center. ^b Subsequent to dehydration. ^c Measured at 890 Torr. ^d Measured at 300 K. ^e The lattice parameter is estimated as ~10.6 Å for **3**, considering the increase in this parameter from 10.16 (**1**) to 10.42 (**2**) due to the increase in the principal quantum number.^{2h}

**Figure 2.** Overlay of the diffuse reflectance spectra for compounds 1–3.

cell parameters are given in Table 1. The broad diffraction peaks observed for **3** are thought to be associated with a smaller size of the crystallites compared with those in **1** and **2**; unfortunately, all efforts to improve crystallinity by varying the synthetic conditions were unsuccessful.

Optical Properties. The UV–vis–NIR diffuse reflectance spectra were measured for compounds 1–3 over the range 4000–40 000 cm⁻¹ (see Figure 2), where $F(R)$ represents the Kubelka–Munk transform. The spectra are characterized by an asymmetrically shaped band between 4000 and 23 000 cm⁻¹, in addition to a number of relatively lower-intensity bands at energies above 23 000 cm⁻¹. The absence of bands in the region 4000–23 000 cm⁻¹ for the mononuclear compounds K₄[Ru(CN)₆] and K₄[Fe(CN)₆] which contain C-coordinated M^{II} centers (see Figure S3, Supporting Information) confirm that the bands present in this region for the framework systems must arise as a result of interactions *between* metal centers. These intervalence charge transfer (IVCT) transitions occur between the formally +2 and +3 metal centers. The higher-energy transitions located above 23 000 cm⁻¹ are also present in the mononuclear complexes, lending support to their assignment as transitions centered at a given metal. It must be noted that the UV–vis–NIR spectra of the mononuclear complexes incorporating C-coordinated M^{III} centers, [M(CN)₆]³⁻, are known to exhibit bands in the region above 20 000 cm⁻¹ only.⁹

The UV–vis spectral properties of Prussian blue, **1**, as well as the unsymmetrical analogues Fe^{III}Ru^{II} (**2**) and Fe^{III}Os^{II} (measured as suspensions in water) have been discussed previously by Robin.^{2a} On the basis of a localized molecular orbital description for **1**, in which the optical electrons are predominantly localized on the Fe^{II} center in the ground state, Robin assigned the transition at 14 200 cm⁻¹ to a transition

from t_{2g}(d⁶) at Fe^{II} to t_{2g}(d⁵) at Fe^{III}. The higher-energy bands situated above 25 000 cm⁻¹ were assigned as t_{2g}(d⁶) to e_g transitions associated with the Fe^{II} centers. Qualitatively, the increase in the degree of electron localization for the series Ru^{III}Ru^{II} ($\nu_{\max} = 9980$ cm⁻¹), Fe^{III}Fe^{II} (16 210 cm⁻¹), and Fe^{III}Ru^{II} (20 180 cm⁻¹) is reflected by the shift of the IVCT bands to successively higher energies.

The characteristics of the IVCT bands—specifically, their energy (ν_{\max}), intensity (ϵ_{\max}), and bandwidth ($\Delta\nu_{1/2}$)—may be quantitatively related to the factors that influence electronic delocalization and the activation barriers to electron transfer, through the seminal two-state classical formalism pioneered by Hush.¹⁰ Of particular significance is the relationship between ν_{\max} and the Franck–Condon reorganization energy (λ), the redox asymmetry (ΔE_0), and additional energy contributions due to spin–orbit coupling and ligand field asymmetry ($\Delta E'$):

$$\nu_{\max} = h\nu = \lambda + \Delta E_0 + \Delta E' \quad (1)$$

The presence of a redox asymmetry component, ΔE_0 in eq 1, for the unsymmetrical Fe^{III}Ru^{II} framework accounts for the high energy of the IVCT band. The relatively broad bandwidths, $\Delta\nu_{1/2}$, compared with the theoretical bandwidths, $\Delta\nu_{1/2}^0$, further support a localized assignment for the frameworks. The broadest IVCT is observed for the Ru^{III}Ru^{II} system, where the low energy tail of the band extends into the mid-IR region, as can be seen from an overlay of the infrared spectra in Figure S1 (Supporting Information). The lower intensity of the IVCT band for **3** relative to **1** is surprising, since the degree of electronic coupling between the metal centers in Ru^{III}Ru^{II} is expected to be greater than that in Fe^{III}Fe^{II}, leading to a relatively more intense band in the former case. The anomaly can be explained on two bases. First, reflectance spectra are sensitive to particle sizes, and the lower overall intensity of the spectrum for **3** may reflect this difference. Repeated measurements on different samples of **3** subjected to different levels of grinding with a mortar and pestle yielded the same intensity spectrum in all cases, however. Second, if the variable particle sizes for samples 1–3 contribute to the difference in the intensities of their spectra, the normalization of the spectra based on their MLCT bands in the region above 30 000 cm⁻¹ will provide for a more accurate comparison of their IVCT bands. Considering this approach, the IVCT band for **3** is increased approximately five times, in which case its relative intensity is higher than that of **1**, as expected.

The results for the band parameters obtained from the Gaussian deconvolution procedure are reported in Table S1

(9) Lever, A. B. P. *Inorganic electronic spectroscopy*; Elsevier: Amsterdam, 1984.

(10) (a) Hush, N. S. *Prog. Inorg. Chem.* **1967**, *8*, 391. (b) Hush, N. S. *Electrochim. Acta* **1968**, *13*, 1005. (c) Buser, H. J.; Schwarzenbach, D.; Petter, W.; Ludi, A. *Inorg. Chem.* **1977**, *16*, 2704.

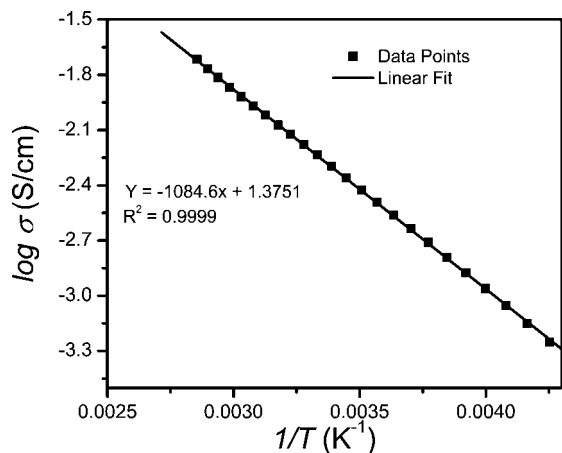


Figure 3. Temperature dependence of the electrical conductivity of **3**, as measured by the four-point probe method.

in the Supporting Information. In the present case, the skewed appearance of the IVCT bands between 4000 and 23 000 cm^{-1} can be rationalized by the contributions of multiple underlying Gaussian-shaped components (see Figure S4, Supporting Information). In the solution phase, Gaussian-shaped IVCT bands had been observed for the $\text{Fe}^{\text{III}}\text{Fe}^{\text{II}}$, $\text{Fe}^{\text{III}}\text{Ru}^{\text{II}}$, and $\text{Fe}^{\text{III}}\text{Os}^{\text{II}}$ Prussian blues,^{2a} and it is likely that the absence of solvent broadening in the solid state spectra permit the resolution of the underlying component transitions. For all three compounds, **1–3**, the IVCT band is comprised predominantly of one major underlying transition with a maximum energy and intensity corresponding to that of the overall band manifold. The lower-energy side of the band is comprised of one (**2** and **3**) or two (**1**) underlying bands. These components may be assigned as spin–orbit transitions which give rise to the $\Delta E'$ component in eq 1 or to a vibronic progression.

Electrical Conductivity. Electrical conductivity measurements were performed on solid samples of **1–3** using the standard four-point probe method. As shown in Figure 3, the conductivity of **3** ($\text{Ru}^{\text{III}}\text{Ru}^{\text{II}}$) is 5.7×10^{-3} S/cm at 300 K and increases to 1.9×10^{-2} S/cm at 350 K. This increase in the conductivity with rising temperature is indicative of a semiconducting material. Significantly, despite its reduced crystallinity, compound **3** exhibits a higher conductivity compared with that of Prussian blue **1** (5.5×10^{-5} S/cm at 300 K) and the unsymmetrical $\text{Fe}^{\text{III}}\text{Ru}^{\text{II}}$ Prussian blue analogue **2** (5.05×10^{-6} S/cm at 300 K). Prussian blue itself is known to exhibit p-type semiconducting behavior, which is based on a hopping conduction mechanism.^{2d–h} The order of the conductivity varies between 10^{-5} S/cm and 10^{-9} S/cm depending on the degree of solvated water, and the conductivity increases with a rise in the potassium content.^{2d} The effects of heating and pressure on the conductivity of Prussian blue have also been reported.¹¹ In the present case, the high conductivity observed for **3** relative to **1** and **2** may arise from the combined effects of solvated water, the higher degree of electronic delocalization, and the presence of potassium ions (which can migrate through interstitial sites

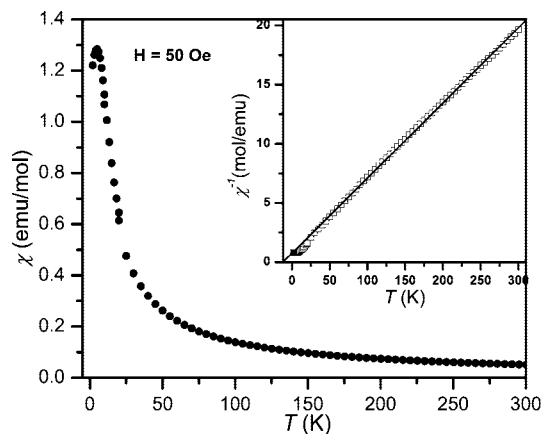


Figure 4. Temperature dependence of the magnetic susceptibility of **2** at 50 Oe. Inset shows the temperature variation of the inverse susceptibility at 50 Oe. The solid line represents the linear fit.

in the lattice while electrons migrate according to the hopping mechanism).

Magnetic Properties. The magnetic properties of **2** are shown in Figure 4. The high temperature inverse susceptibility data recorded at 50 Oe (see Figure 4, inset) give a Weiss temperature of -12 K, suggesting that the dominant exchange interactions are antiferromagnetic. The effective magnetic moment per iron center is $5.7 \mu_{\text{B}}$, which is close to the value of $5.9 \mu_{\text{B}}$ expected for the $S = 5/2$ ground-state associated with high-spin Fe^{III} in an octahedral coordination environment and to the value for Prussian blue ($5.8 \mu_{\text{B}}$).¹² It is well-known that Prussian blue shows ferromagnetic ordering at 5.6 K through a double-exchange mechanism that involves valence delocalization in the ground-state between Fe^{II} and Fe^{III} .¹³ While a similar exchange mechanism may be expected for **2**, the increase in the lattice parameter due to the larger principal quantum number (10.16 Å for **1** versus 10.42 Å for **2**)^{2h} may hinder the electronic exchange interaction through the cyanide bridging ligand. Furthermore, no magnetic hysteresis was observed at 1.8 K (see Figure S5, Supporting Information).

Compound **3** exhibits a Weiss temperature of -6.8 K, suggesting that the ruthenium centers are antiferromagnetically coupled. The effective magnetic moment was determined to be $1.69 \mu_{\text{B}}$ per Ru^{III} , which is close to the value typically observed for low-spin Ru^{III} ($S = 1/2$, $1.71 \mu_{\text{B}}$) in an octahedral coordination environment.¹⁴ Unexpectedly, particularly in the face of the apparent increase in electron delocalization evident in the optical spectra, the all-ruthenium Prussian blue analogue **3** does not show a magnetic ordering transition at temperatures down to 1.8 K (see Figure S6, Supporting Information).

Gas Adsorption Properties. In recent work, N_2 adsorption measurements performed at 77 K on Prussian blue (**1**) after degassing at 40 °C for 60 h revealed a type I adsorption isotherm typical of a microporous solid and a BET surface

(11) (a) Inoue, H.; Nakazawa, T.; Mitsuhashi, T.; Shirai, T.; Fluck, E. *Hyperfine Interact.* **1989**, *46*, 725. (b) Hara, Y.; Minomura, S. *J. Chem. Phys.* **1974**, *61*, 5339.

(12) (a) Ito, A.; Suenaga, M.; Ono, K. *J. Chem. Phys.* **1968**, *48*, 3597. (b) Bauser, H. J.; Ludi, A.; Fisher, P.; Studach, T.; Dale, B. W. *Z. Phys. Chem.* **1974**, *92*, 354.

(13) Mayoh, B.; Day, P. *J. Chem. Soc., Dalton Trans.* **1976**, 1486.

(14) (a) Harzion, Z.; Navon, G. *Inorg. Chem.* **1982**, *21*, 2606. (b) Bai, L.-X.; Liu, X.; Wang, W.-Z.; Liao, D.-Z.; Wang, Q.-L. *Z. Anorg. Allg. Chem.* **2004**, *630*, 1143.

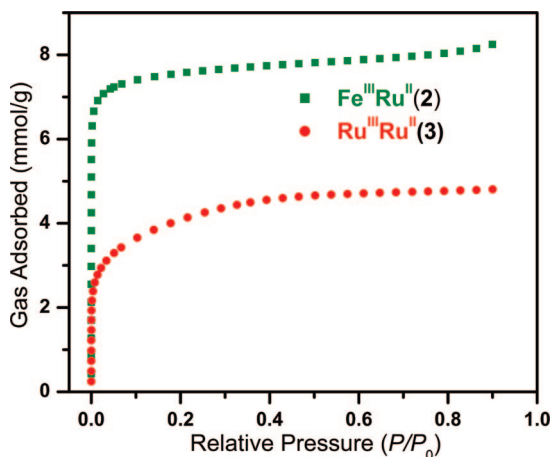


Figure 5. Nitrogen adsorption isotherms for **2** and **3** collected at 77 K.

area of 550 m²/g.^{4e} Hydrogen adsorption measurements showed a fully reversible uptake of 1.2 wt % at 77 K and 890 Torr.^{4e} Upon degassing at 75 °C for 72 h under dynamic vacuum, the N₂ adsorption data at 77 K for **2** and **3** (see Figure 5) also reveal type I isotherms, with BET surface areas of 670 and 325 m²/g, respectively. In the case of **2**, wherein the [Fe(CN)₆]⁴⁻ units in **1** are replaced by [Ru(CN)₆]⁴⁻, the increased surface area may be attributed to the slightly larger unit cell, together perhaps with an enhanced stability against framework collapse. Consistently, this compound exhibits a slightly higher H₂ uptake of 1.4 wt % at 77 K and 890 Torr (see Figure S2, Supporting Information). In contrast, the significantly lower surface area observed for the all-ruthenium Prussian blue analogue **3**, likely arises from a combination of factors involving a reduction in the concentration of framework vacancies, the presence of K⁺ cations in the pores, and the heavier atomic weight of ruthenium. Accordingly, this compound displays an uptake of just 0.5 wt % H₂ at 77 K and 890 Torr.

Conclusions

Ruthenium and iron–ruthenium Prussian blue analogues have been synthesized and characterized by optical, electrical conductivity, magnetic susceptibility, and gas adsorption measurements. The increase in the degree of electronic localization for the unsymmetrical iron–ruthenium analogue Fe₄[Ru(CN)₆]₃·18H₂O (**2**) relative to Prussian blue (Fe₄[Fe(CN)₆]₃·14H₂O, **1**) is reflected in a shift of the IVCT band to higher energies and a decrease in the electrical conductivity. Contrastingly, the symmetrical all-ruthenium analogue K_{1.2}Ru_{3.6}[Ru(CN)₆]₃·16H₂O (**3**) exhibits a lower-energy IVCT band, consistent with an increased electronic delocalization and a higher electrical conductivity. Unlike Prussian blue which exhibits magnetic ordering at 5.6 K, compounds **2** and **3** show no signs of magnetic ordering above 1.8 K. The presence of mixed valency in three-dimensional coordination frameworks is a highly sought-after property, and the foregoing studies of the IVCT and conductivity properties of Prussian blue analogues provide a step toward the realization of microporous materials with potentially wide-ranging applications as lightweight conductors and chemical sensors via conductivity changes, and potentially as thermoelectric materials and battery components.

Acknowledgment. This research was funded by the Laboratory Directed Research and Development Program of Lawrence Berkeley National Laboratory under the Department of Energy Contract No. DE-AC02-05CH11231. We thank the American Australian Association and the 1851 Royal Commission for support of DMD through postdoctoral fellowships.

Supporting Information Available: Details of the spectral analysis, deconvoluted spectra, and infrared spectra of **1**–**3**. Hydrogen adsorption isotherms and TGA data for **2** and **3**. Magnetization data for **2** and magnetic susceptibility and magnetization data for **3** (PDF). This material is available free of charge via the Internet at <http://pubs.acs.org>.

CM900230P